JGR Oceans

RESEARCH ARTICLE
10.1029/2025JC023156

Fetch-Dependent Surface Wave Responses to Offshore Wind Farms in the Northeast U.S. Coast

César Sauvage[1], **Hyodae Seo**[1], **Seth Zippel**[2], **Carol Anne Clayson**[3], **and James B. Edson**[3]

[1]University of Hawai'i, Honolulu, HI, USA, [2]Oregon State University, Corvallis, OR, USA, [3]Woods Hole Oceanographic Institution, Woods Hole, MA, USA

Key Points:

- Surface wind speed is reduced up to 10% in the wind farm wake while wave height and wave-supported stress are decreased by 3% and 30%
- The lower wind-sea energy suggests reduced wave growth in the vicinity of the wind farms
- Weaker winds favor the presence of longer-period waves, altering the local wave regime and further reducing the ocean surface roughness length

Supporting Information:

Supporting Information may be found in the online version of this article.

Correspondence to:

C. Sauvage,
csauvage@hawaii.edu

Citation:

Sauvage, C., Seo, H., Zippel, S., Clayson, C. A., & Edson, J. B. (2025). Fetch-dependent surface wave responses to offshore wind farms in the Northeast U.S. Coast. *Journal of Geophysical Research: Oceans*, *130*, e2025JC023156. https://doi.org/10.1029/2025JC023156

Received 17 JUL 2025
Accepted 6 DEC 2025

Author Contributions:

Conceptualization: César Sauvage, Hyodae Seo
Formal analysis: César Sauvage
Funding acquisition: Hyodae Seo, Seth Zippel, Carol Anne Clayson, James B. Edson
Investigation: César Sauvage
Methodology: César Sauvage, Hyodae Seo
Project administration: Hyodae Seo
Software: César Sauvage, Hyodae Seo
Supervision: Hyodae Seo
Validation: César Sauvage
Visualization: César Sauvage
Writing – original draft: César Sauvage, Hyodae Seo
Writing – review & editing: César Sauvage, Hyodae Seo, Seth Zippel, Carol Anne Clayson, James B. Edson

Abstract Large-scale offshore wind farms are expected to influence surface waves by modifying local wind forcing through wake effects. We use regional coupled ocean-atmosphere-wave model simulations to investigate a realistic large-scale offshore wind development scenario in the northeastern U.S. during boreal summer. Near-surface wind speeds are reduced by 10% over lease areas and within downstream wake regions, leading to decreases in significant wave height (3%) and wave-supported momentum flux (30%). This further leads to reductions in surface roughness length (16%) and near-surface ocean turbulent kinetic energy (20%). Spectral analysis shows a clear reduction in wind-sea energy, indicating suppressed local wind-wave growth near the wind farms. Weaker winds favor the development of longer-period waves, increasing dominant wave phase speed by 3% and suggesting a transition to an older sea state. Modern bulk flux algorithms often parameterize surface roughness using inverse wave age and/or wave slope. This raises the question of whether wake-driven reductions in inverse wave age and wave height impact air-sea momentum exchange. To assess this, we compare fully coupled simulations with an atmosphere-only run excluding wave coupling. Results show that about one-third of the reduction in roughness length can be attributed to sea state changes, while two-thirds result from lower friction velocity due to lower wind speeds. However, the impact of sea state on the drag coefficient and momentum flux is negligible (∼1%), suggesting that wake-induced wind speed reductions are the primary driver, with sea state changes playing a secondary role.

Plain Language Summary Offshore wind farms are designed to generate clean energy, but they also change how winds behave over the ocean. When wind turbines extract energy from the air, they slow down the wind behind them, creating a "wake." In this study, we used computer models to explore how these changes in wind may affect ocean waves off the northeastern United States during summer. We found that winds decrease in and around wind farm areas. Since wind is the main source of energy for wave growth, this weakening leads to slightly smaller waves and lowers the energy transfer between the atmosphere and the ocean waves. The types of waves also change; choppier, rougher waves become less common, while longer, smoother swell waves appear more frequently. The shape and size of waves can affect how much energy and momentum the wind transfers to the ocean. To understand how much of the overall changes are due to the waves themselves, we compared two model setups, one with waves included and one without. We found that most of the changes were caused by weaker winds, while the change in wave patterns only played a smaller, secondary role.

1. Introduction

Offshore wind farms in the northeastern United States play a vital role in the region's transition to renewable energy. By converting the kinetic energy of wind to electricity, these large-scale installations of wind turbines in coastal ocean environments are also known to alter near-surface wind patterns. The extent to which wind turbines modify near-surface meteorology, surface winds, and atmospheric boundary layer profiles has been the subject of extensive investigations in recent years (e.g., Akhtar et al., 2021, 2022; Bodini et al., 2019, 2021; Fischereit, Brown, et al., 2022; Golbazi et al., 2022; Quint et al., 2024, 2025; Raghukumar et al., 2022; Rosencrans et al., 2024). For example, a regional study by Quint et al. (2024) found that wind farms significantly reduce wind speeds both at hub height and at 10 m, and the magnitudes of these responses are strongly dependent on prevailing atmospheric stability conditions.

Because of the strongly coupled nature of the surface waves and surface winds, these changes in wind fields are expected to modify surface wave characteristics, including energy, mean and peak frequency, and direction (e.g., Bärfuss et al., 2021; Christensen et al., 2014; Fischereit, Brown, et al., 2022; Larsén et al., 2024; McCombs et al., 2014; L. Wu et al., 2020). In the North Sea, previous studies using in situ observations and coupled modeling experiments (Bärfuss et al., 2021; Larsén et al., 2024) have shown that wind wakes reduce significant wave height and wave energy downstream of the wind farm. Evidence exists that these changes also impact near-surface ocean turbulent kinetic energy (TKE), upper-ocean mixing and stratification, and sea surface temperature, particularly in seasonally stratified shelf regions (Benkort et al., 2024; Broström, 2008; Christiansen, Daewel, Djath, & Schrum, 2022; Christiansen, Daewel, & Schrum, 2022; Daewel et al., 2022; Dorrell et al., 2022; Floeter et al., 2022; Paskyabi & Fer, 2012).

Offshore wind farms may also affect wave conditions through interaction involving turbine foundations and wake-induced ocean currents (e.g., Alari & Raudsepp, 2012; Carpenter et al., 2016; Christiansen et al., 2023; Hosseini et al., 2025; Ludewig, 2015; Ponce de León et al., 2011; Schultze et al., 2020; Zhao et al., 2024). However, such mechanisms are not considered in this study, which focuses specifically on wind wake-induced effects on surface waves.

Understanding the influence of offshore wind farms on ocean surface waves via the wind wake effect is important from the air-sea interaction perspective, as momentum exchange across the atmospheric and oceanic boundary layers is primarily supported by strongly coupled wind waves with wavelengths on the order of $\mathcal{O}(0.1\text{–}10\ \text{m})$ (Edson et al., 2013; Sullivan et al., 2014, 2018). In numerical models, air-sea momentum exchanges are generally represented through the roughness length parameterization, which depends either solely on the surface wind speed or a combination of wave characteristics such as wave age, wave slope, and wave direction (e.g., Edson et al., 2013; Sauvage et al., 2023; Taylor & Yelland, 2001). Thus, by altering near-surface wind fields and ocean surface wave characteristics (Fischereit, Larsén, & Hahmann, 2022; Golbazi & Archer, 2019; Larsén et al., 2024), offshore wind farms may modulate the air-sea momentum flux. Furthermore, wave-modulated surface stress can influence the kinematic and thermodynamic structure of the marine atmospheric boundary layer, with implications for turbine wake development and power generated by the wind farms (AlSam et al., 2015; Deskos et al., 2021; Kalvig et al., 2014; Ning & Paskyabi, 2024; Ning et al., 2023; Porchetta, Muñoz-Esparza, et al., 2021; Porchetta, Temel, et al., 2021; L. Wu et al., 2020; C. Wu et al., 2022; Yang et al., 2022). However, the extent to which the wake-induced surface wave changes feed back to the atmospheric boundary layer and power output is not well understood.

Thus, this study investigates the surface wave response to a realistic scenario of large-scale offshore wind farm development in the northeastern U.S continental shelf from the viewpoint of air-sea momentum exchanges. Our analysis based on high-resolution fully coupled ocean-atmosphere-wave model simulations focuses on the boreal summer season. We focus on this season because it features relatively stable atmospheric conditions and pronounced turbine wake effects (e.g., Bodini et al., 2021; Quint et al., 2024), conditions that facilitate a clearer assessment of ocean wave response to the wind farm wake effect.

The high-resolution coupled modeling framework is described in Section 2. Section 3 presents the main results based on simulations conducted with and without wind farms. In Section 3.1, we examine how reduced near-surface wind speeds associated with wind farms lead to decreases in wind-sea energy and wind stress. Section 3.2 demonstrates that suppressed wind-wave growth causes a spectral shift toward longer-period swell waves. In Section 3.3, we find that this shift to aerodynamically smoother, swell-dominated conditions reduces wave-supported roughness length and momentum flux. However, we also show that this effect is secondary to the reduction in wind stress directly caused by wind speed deficits in turbine wakes. A summary of these findings is provided in Section 4.

2. Method

2.1. Regional Coupled Modeling

This study utilizes the Scripps Coupled Ocean-Atmosphere Regional (SCOAR) modeling system (Sauvage et al., 2023, 2024; Seo et al., 2007), which integrates the Weather Research and Forecasting (WRF) model (Skamarock et al., 2021) for the atmosphere with the Regional Ocean Modeling System (ROMS) (Haidvogel et al., 2000; Shchepetkin & McWilliams, 2005) for the ocean and the third-generation spectral wave model WaveWatch III (WW3) (Tolman et al., 2002) for surface waves.

In this study, WRF employs a one-way nesting approach, with horizontal grid spacing refined from 7.5 km in the outer domain to 1.5 km in the nested domain (Figure 1). The vertical grid consists of 50 levels, with 20 levels

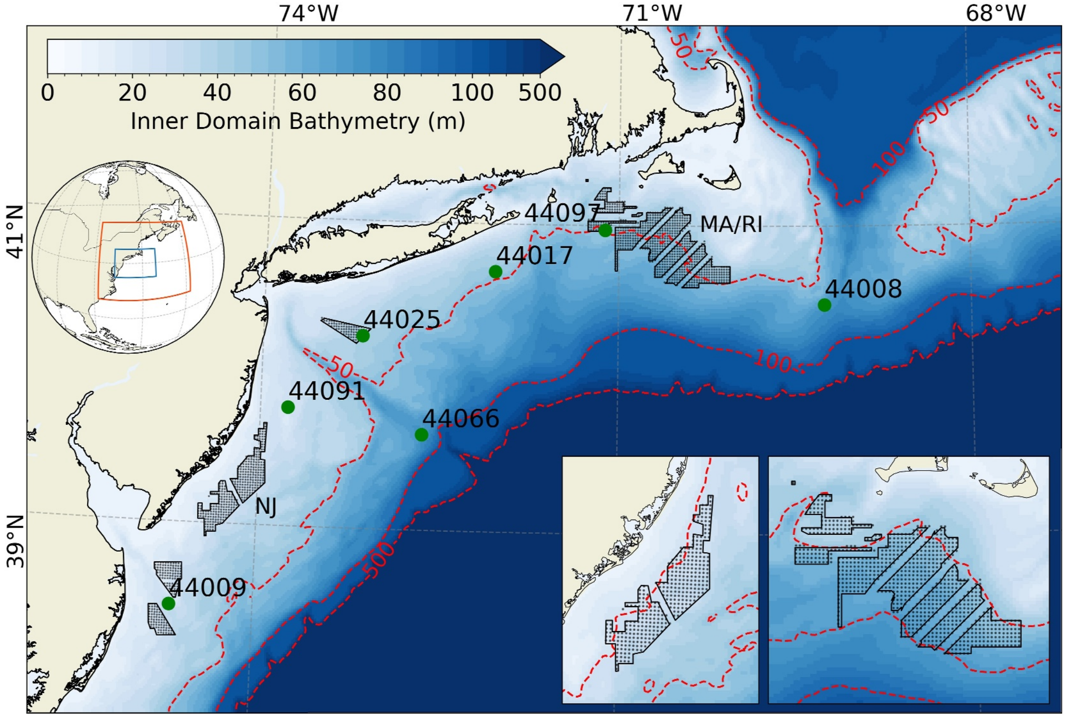

Figure 1. The nested coupled domain with shelf bathymetry up to 500 m depth, shaded in meters. The dashed red lines represent the 50-, 100-, and 500-m isobaths. The solid black contour lines show the location of the wind farms. The two largest lease areas, Massachusetts/Rhode Island (MA/RI) and New Jersey (NJ), respectively, containing 830 and 464 turbines, are shown in close-ups in the lower right corner. Green dots correspond to National Data Buoy Center (NDBC) mooring locations. The inset at the upper left shows the outer model domain and the inner fully coupled domain.

below 250 m. The lowest level of the model layer is centered at 5.5 m, and the second level at 12 m. The outer WRF domain dynamically downscales the ERA5 reanalysis (Hersbach et al., 2020) and is run with spectral nudging to retain the low-wave number characteristics of the downscaled circulation close to those in ERA5. In the inner domain, which is not nudged, atmospheric processes are resolved at 1.5 km resolution. WRF in the nested domain is coupled with ROMS and WW3. ROMS is driven by the daily 1/12° MERCATOR International global reanalysis (Lellouche et al., 2018) and WW3 by 14 spectral points obtained from the global 1/2° WW3 simulations (Rascle & Ardhuin, 2013). These three models share identical grids and land-sea masks and are coupled hourly. A detailed description of the physical parameterizations and schemes used in the model is provided in Table 1.

Air-sea momentum, heat, and freshwater fluxes are computed using the COARE wave-based bulk flux algorithm (Edson et al., 2013; Fairall et al., 1996, 2003), integrated within the Mellor-Yamada-Nakanishi-Niino (MYNN) surface layer scheme (Olson et al., 2021). In addition to standard meteorological outputs from WRF, sea surface temperature, and surface currents from ROMS, the COARE wave-based formulation utilizes peak wave phase speed (c_p) and significant wave height (H_s) from WW3 to estimate the surface roughness length (z_0) (Edson et al., 2013), given by

$$z_0 = z_0^{rough} + z_0^{smooth} = H_s 0.09\left(\frac{u_*}{c_p}\right)^2 + 0.11\,\frac{\nu}{u_*}, \tag{1}$$

where u_* is the friction velocity and ν the kinematic viscosity. At the wind speed ranges considered in this study (Figures 2 and 3a), z_0 is dominated by the first term, representing the roughness elements driven by the wind stress in the form of surface gravity waves. As wind farms modify sea state characteristics such as c_p and H_s by lowering wind speeds through wake effects, we examine the corresponding changes in the parameterized z_0 and consequently in the drag coefficient (C_D), wave-supported stress (τ_{aw}) and the total momentum flux (τ). In addition to

Table 1
Model Physics

Model	Parameter	Physics details
WRF	Time step	20 s, 4 s
	Horizontally	7.5 km and 1.5 km
	Vertically	50 levels, with 20 below 250 m. 1^{st} model level is at 5.5 m and 2^{nd} is at 12 m
Outer domain only	Forcings	Hourly $0.25\circ$ ERA5 (Hersbach et al., 2020)
	Spectral nudging	Above the PBL to zonal and meridional wavelengths longer than 850 km and 730 km
	Deep convection	Kain-Fritsch (Kain, 2004), outer domain only
	Cloud microphysics	Thompson (Thompson et al., 2008)
	Land surface	NOAH-LSM (Tewari et al., 2004)
	Radiations	RRTM (Iacono et al., 2008)
	PBL	MYNN 2.5 (Nakanishi & Niino, 2009)
	Surface layer	MYNN (Olson et al., 2019, 2021)
	Wind farm	1,418 wind turbines, Fitch Param. (Fitch et al., 2012)
ROMS	Time step	60 s
	Horizontally	1.5 km
	Vertically	30-level stretched vertical grid $\theta_s = 7$, $\theta_b = 2$, $h_{\text{cline}} = 300$ m, and $h_{\min} = 10$ m
	Bathymetry	GEBCO $1'$(Weatherall et al., 2015)
	Forcings	Daily $1/12\circ$ MERCATOR (Lellouche et al., 2018)
	Vertical mixing	GLS k-ϵ (Warner et al., 2005)
	Stability function	Canuto-B (Canuto et al., 2001)
	Horizontal adv.	3rd-order upstream-biased
	Vertical adv.	4th-order centered differences
	Bottom drag	Quadratic drag
	Tides	OSU Tidal Prediction Software (Egbert & Erofeeva, 2002)
WW3	Time step	180 s
	Horizontally	1.5 km
	Spectrum	32 frequencies, 24 directions, $FREQ_1 = 0.0373$ Hz, and $X_{fr} = 1.1$
	Boundaries	14 spectral points from global hindcast (Rascle & Ardhuin, 2013)
	Initial conditions	End states of a 30-day spin-up simulation forced by ERA5
	Source term	ST4 package (Ardhuin et al., 2009, 2010)
	Wave reflection	Enables reflection of shorelines (Ardhuin & Roland, 2012)
	Depth-induced breaking	Battjes-Janssen model (Battjes & Janssen, 1978)
	Bottom friction	SHOWEX bottom friction formulation (Ardhuin et al., 2003)

spectrally averaged wave outputs, full directional wave spectra are saved every 15 km across the domain. These outputs are used to illustrate the spatial distribution and fetch dependence of the spectral changes in wave fields.

The effects of wind turbine wakes in the WRF nested domain are represented using the Fitch parameterization (Fitch et al., 2012) as implemented in the MYNN planetary boundary layer (PBL) scheme (see Section 2.2). A series of coupled and complementary uncoupled model simulations is conducted. First, two fully coupled ocean-atmosphere-wave model simulations are performed: a control run without the wind farm parameterization (NOWF, unperturbed case) and a simulation incorporating the wind farm parameterization (WF). The lease areas (i.e., the areas leased by wind farm developers) are shown in Figure 1. In addition, a set of WRF-only simulations (WF_NWC) is carried out to isolate the effect of sea state modifications on momentum fluxes. All simulations span five boreal summer seasons (June, July, and August, JJA) for 2017–2021.

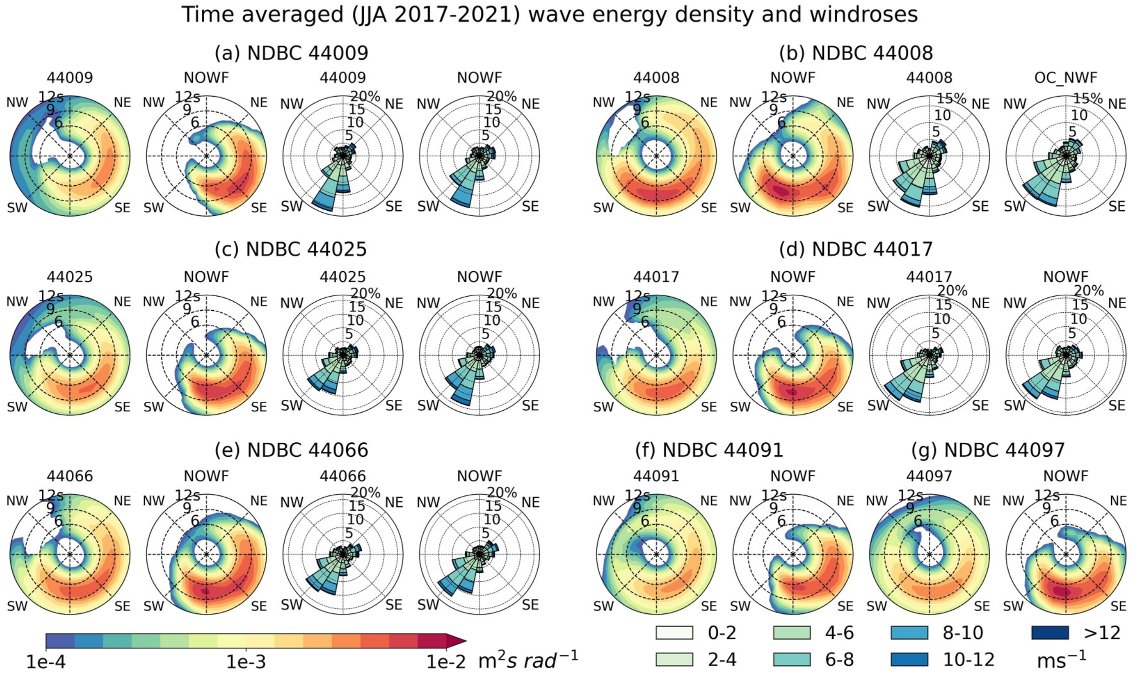

Figure 2. Time-averaged (JJA, 2017–2021) wave energy density (m^2 s rad^{-1}) and surface wind speed (m s^{-1}) from several National Data Buoy Center (NDBC) moorings (a) 44009, (b) 44008, (c) 44025, (d) 44017, (e) 44066, (f) 44091, and (e) 44097 against the corresponding simulated quantities in the unperturbed simulation (NOWF). Both NDBC 44091 and 44097 moorings are not equipped with anemometers and therefore do not measure wind speed. Exact locations are shown on Figure 1.

2.2. Wind Farm Parameterization

Wind turbine wake effects are represented using the Fitch parameterization (Fitch et al., 2012), incorporating the updates recommended by Archer et al. (2020). In this scheme, wind turbines act as momentum sinks and sources

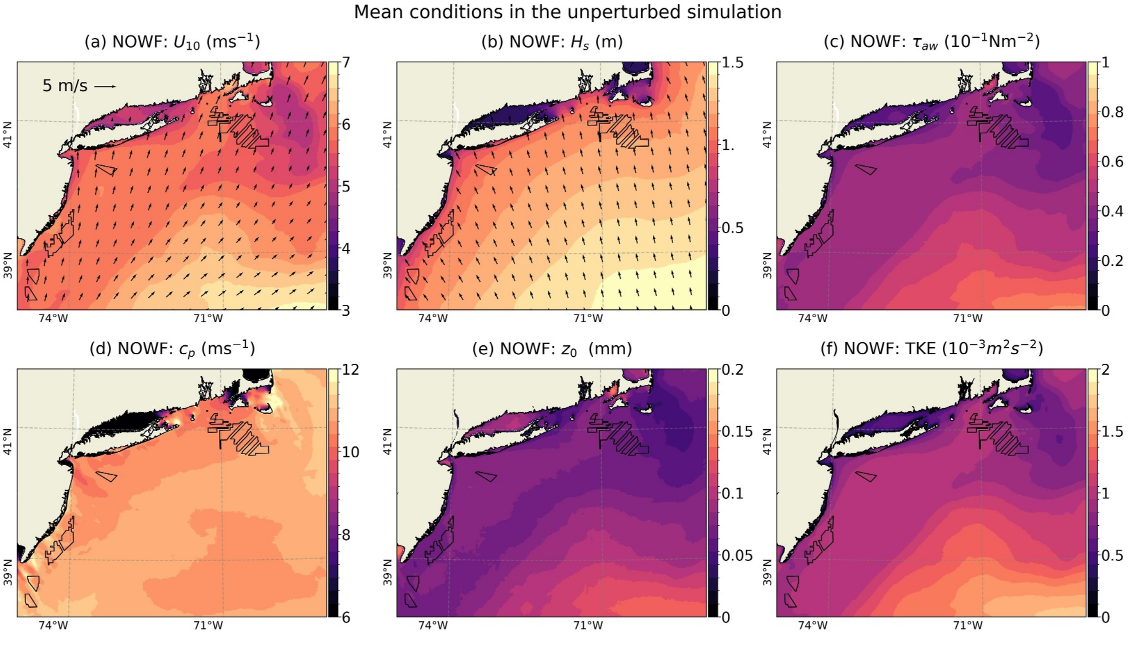

Figure 3. Time-averaged (JJA, 2017–2021) from the unperturbed simulation (NOWF) for (a) 10 m wind speed (U_{10}, m s^{-1}), (b) significant wave height (H_s, cm), (c) wave-supported stress (τ_{aw}, 10^{-2} N m^{-2}), (d) wave peak phase speed (c_p, m s^{-1}), (e) ocean surface roughness length (z_0, mm), and (f) ocean turbulent kinetic energy (TKE, $10^{-3}\mathrm{m}^2$ s^{-2}). Black arrows represent (a) the wind speed direction and (b) the peak wave direction.

of TKE at the model levels intersecting the rotor-swept area. The TKE generated by turbines is not computed directly within the Fitch scheme but is prescribed to the scheme as a parameter, α (Archer et al., 2020).

Previous studies have shown that simulated wake characteristics are sensitive to the choice of α, which determines the fraction of turbine-generated TKE added to the model (Archer et al., 2020; Bodini et al., 2021; Fischereit, Brown, et al., 2022; Larsén & Fischereit, 2021; Rosencrans et al., 2024). The default value $\alpha = 0.25$ assumes that 25% of the turbine-produced TKE is injected into the atmosphere; however, several studies have demonstrated that model sensitivity varies across different environments and conditions (Ali et al., 2023; Larsén et al., 2024). To evaluate the robustness of the simulated wave response to this parameter, two configurations are tested: $\alpha = 0.25$ (WF) and $\alpha = 1.0$ (WF_100).

Turbine characteristics, including dimensions, power and thrust coefficients, and layout configurations, follow those described by Rosencrans et al. (2024). A total of 1,418 turbines are distributed across the Mid-Atlantic Bight lease areas (Figure 1). Each turbine has a rated capacity of 12 MW, a hub height of 138 m, and a rotor diameter of 215 m, corresponding to blade tip heights of 30.5 m (bottom) and 245.5 m (top). In WRF, 15 vertical model levels intersect the rotor-swept region, with an additional 4 levels below the lowest blade tip. This fine vertical resolution is essential for accurately resolving turbine wake effects within the atmospheric boundary layer (Tomaszewski & Lundquist, 2020).

2.3. Wave Spectrum Partitioning

Wave spectrum partitioning is performed offline using an algorithm available through the "Wavespectra" open source Python library and is based on the method used in WW3 model (The WAVEWATCH III Development Group, 2019; Tracy et al., 2007). Wind-sea and swell components are defined using a topographic partitioning method, which groups spectral bins into distinct wave systems. These systems are then classified according to a wind-sea fraction cutoff (Hanson & Phillips, 2001; Hanson et al., 2009; Portilla et al., 2009; Vincent & Soille, 1991). First, the spectrum is divided into different partitions representing energy from subpeaks within the spectral distribution. Each partition is characterized by parameters such as wave height, peak period, peak wavelength, and wind-sea fraction. The influence of wind is then quantitatively determined from the wave-age relationship, defined as

$$c_{ws} < \chi_{fac}\, U_{10} \cos(\theta_{ws}), \tag{2}$$

where c_{ws} is the phase speed of the wind sea. The wind-sea region is then defined as the component of the wind speed (U_{10}) in the wave direction, multiplied by the wave age factor χ_{fac}, with θ_{ws} being the angle between the wind direction and that of the wind sea. Thus, any wave components traveling at a phase speed slower than c_{ws} are considered to be wind-forced and initially classified as wind sea. Then, topographic partitions in which the proportion of wind-sea energy exceeds a defined threshold (W_{cut}) are grouped and assigned to the wind-sea component. The value of W_{cut} enables classification of each partition as pure wind-sea ($W_{cut} = 1$), pure swell ($W_{cut} = 0$), or mixed sea states. Remaining partitions are categorized as swell components in order of decreasing wave height.

In this study, we define only one wind-sea and one main swell partition, using the standard values of $W_{cut} = 0.33$ and $\chi_{fac} = 1.7$. While the results of the partitioning process are sensitive to the selection of W_{cut} and χ_{fac}, the overall conclusions of this study remain robust under reasonable variations of these parameters.

2.4. Statistical Significance Method

A two-sided Student's t test was employed to evaluate the statistical significance of time-mean differences between simulations. The effective sample size, n', accounting for temporal autocorrelation within each time series, is computed following Bretherton et al. (1999). Since the time series is segmented by year, n' is computed separately for each summer and then summed to obtain a final n' for the entire period. Statistical significance is assigned only when the final p value indicates significance at the 99% confidence level ($p < 0.01$) and is represented as stippling on the figures, plotted every 6th grid point.

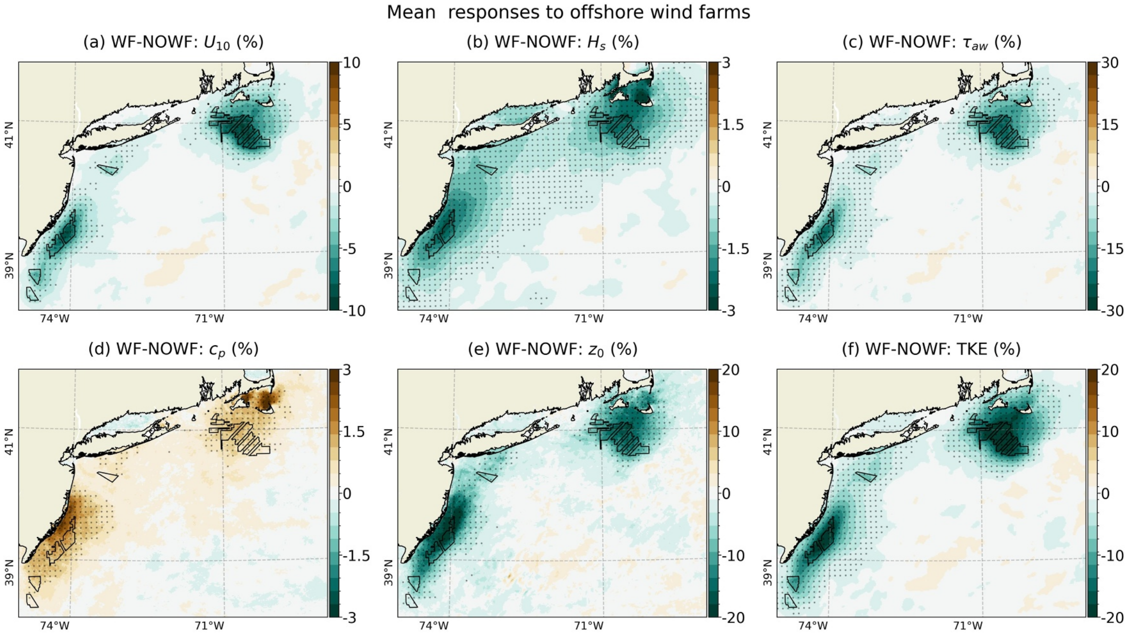

Figure 4. Time-averaged (JJA, 2017–2021) differences WF − NOWF in percent (%) for (a) 10 m wind speed (U_{10}), (b) significant wave height (H_s) (c) wave-supported stress (τ_{aw}), (d) wave peak phase speed (c_p), (e) ocean surface roughness length (z_0), and (f) ocean turbulent kinetic energy (TKE). Statistically significant responses at the 99% confidence level are marked with gray dots.

2.5. In Situ Data

In order to validate simulated surface wind and wave summer characteristics, we use several National Data Buoy Center (NDBC) buoys located off the New England coast (Figure 1). These buoys provide near-surface meteorological and oceanographic measurements, including wave energy spectra and near-surface wind speeds. The in situ observations are compared in Figure 2 with JJA 2017–2021 time-averaged results from the unperturbed simulation (NOWF). Observed surface wind speeds from NDBC buoys are adjusted to the standard height of 10 m using the COARE3.5 bulk flux algorithm (Edson et al., 2013).

3. Results

3.1. Mean Sea State Responses to Offshore Wind Farm

During summer, the Northeast U.S. experiences predominantly southwesterly winds, with moderate near-surface wind speeds of 5–6 ms^{-1} (Figure 2). The long-fetch conditions in the southwest direction allow the wind waves to develop before reaching the Massachusetts/Rhode Island (MA/RI) and New Jersey (NJ) lease areas, resulting in peak periods of approximately 6–8 s (Figure 2). In contrast, waves from the north-northwest are almost nonexistent during summer due to the limited fetch in that direction.

The directional wave spectra in Figure 2 also indicate greater wave energy coming from the south to southeast direction. This is consistent with the longer fetch in that direction, allowing for waves to grow and carry a larger amount of energy. These southeasterly waves typically have longer periods (8–10 s) and are decoupled from the prevailing southwesterly winds. The unperturbed simulation (NOWF) reproduces these observed seasonal patterns reasonably well, capturing both the surface wind characteristics and the general sea state seen in moored observations (Figures 2, 3a, and 3b).

With wind farms (WF) in place, near-surface wind speed (U_{10}) decreases by 10%, or about 0.5 m s^{-1} of the unperturbed values (NOWF), most strongly around the lease areas (Figure 4a). The time-mean surface wave response is spatially well aligned with the wake patterns (Figure 4). As U_{10} weakens, H_s decreases by 3% or about 3 cm of the unperturbed value, while τ_{aw} drops by almost 30% (1.10^{-2}N m^{-2}) (Figures 4b and 4c). Furthermore, c_p increases by 3% (0.3 m s^{-1}) within the wind farm and wake regions (Figure 4d). This suggests that reduced

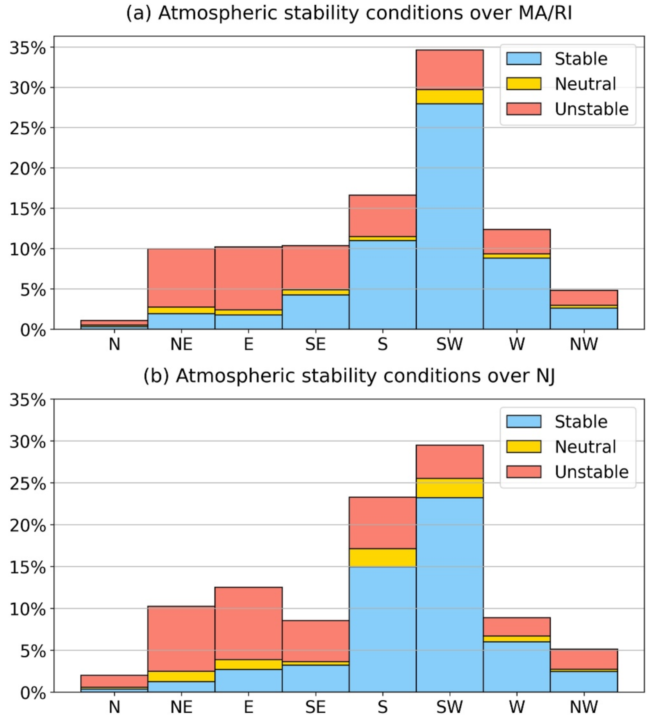

Figure 5. Histogram of averaged wind direction over (a) MA/RI and (b) NJ lease areas, colored by atmospheric stability classification. The atmospheric stability is determined using the Monin-Obukhov length (L). Southwesterly wind composite over MA/RI (NJ) represents 34.7% (29.4%) of the hourly data, southerly about 16.7% (23.3%), westerly about 12.2% (8.4%), southeasterly about 10.4% (8.7%), easterly about 10.2% (12.2%), northeasterly about 9.9% (10.7%), northwesterly about 4.7% (5.1%), and northerly about 1.1% (1.9%).

surface winds suppress local wind-wave growth, which promotes the occurrences of longer-period waves. This phenomenon is explored further in subsequent sections.

It is noteworthy that the largest c_p differences occur in Nantucket Sound, a shallow (10–15 m) region characterized by strong tidal forcing. The local wave field there is further modulated by island sheltering effect, particularly under prevailing southwesterly winds, while weaker modulation is observed under other wind conditions (see also Figure 6).

In response to the decrease in τ_{aw}, z_0 is also decreased up to 20% (1×10^{-2}mm) (Figure 4e). Finally, the near-surface ocean TKE decreases by more than 20% ($0.2 \times 10^{-3}\mathrm{m}^2\ \mathrm{s}^{-2}$), suggesting further changes in breaking waves, turbulence, and mixing in the near-surface ocean (Figure 4f).

The reduction in near-surface wind speeds due to wind farms is consistent with previous studies (i.e., Golbazi et al., 2022; Larsén et al., 2024; Quint et al., 2024; Rosencrans et al., 2024). These studies also suggested that the magnitude of wind speed reductions varies with atmospheric stability and the α parameter in the Fitch scheme (i.e., Archer et al., 2020; Bodini et al., 2021). To assess the sensitivity of our results to these two factors, we compare simulations with different α and classify the prevailing atmospheric stability conditions using the hourly Monin-Obukhov length (Monin & Obukhov, 1954), following the approach of Rosencrans et al. (2024).

Our analysis shows that stably stratified conditions occur most frequently (59.3%) in the unperturbed case (NOWF) (Figure 5), typically associated with winds having a westerly component. Conversely, unstably stratified conditions occur 35.6% of the time in association with easterly winds. These results are similar in the MA/RI and NJ lease areas.

Figures 6 and 7 compare the near-surface wind speed and wave responses under stable and unstable atmospheric conditions. Under stable conditions, wake-induced wind reductions extend farther downstream (Quint et al., 2024), leading to decreases in H_s and τ_{aw} and an increase in c_p. In contrast, under unstable conditions, wind deficits are largely confined within the lease areas, with minimal or no downstream wake effects. Similar patterns of changes are found with H_s, τ_{aw}, and c_p.

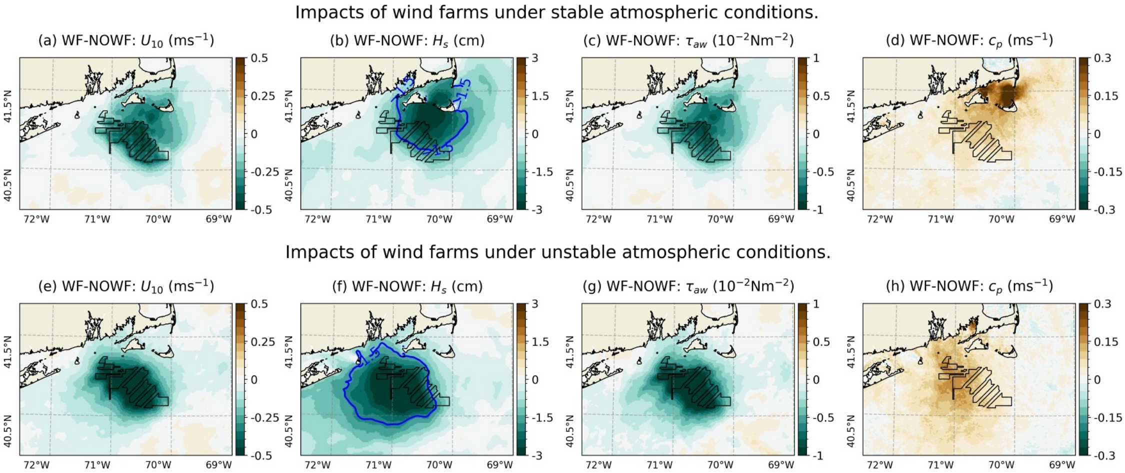

Figure 6. WF − NOWF differences during atmospheric (top row, a–d) stable conditions, based on westerly wind component over MA/RI and (bottom row, e–h) unstable conditions, based on easterly wind component over MA/RI of (a–e) 10 m wind speed (U_{10}, m s^{-1}), (b–d) significant wave height (H_s, m), (c–g) wave-supported stress (τ_{aw}, N m^{-2}), and (d–h) wave peak phase speed (c_p, m s^{-1}). The blue contour on (b) and (f) represents 1.5% decrease in H_s.

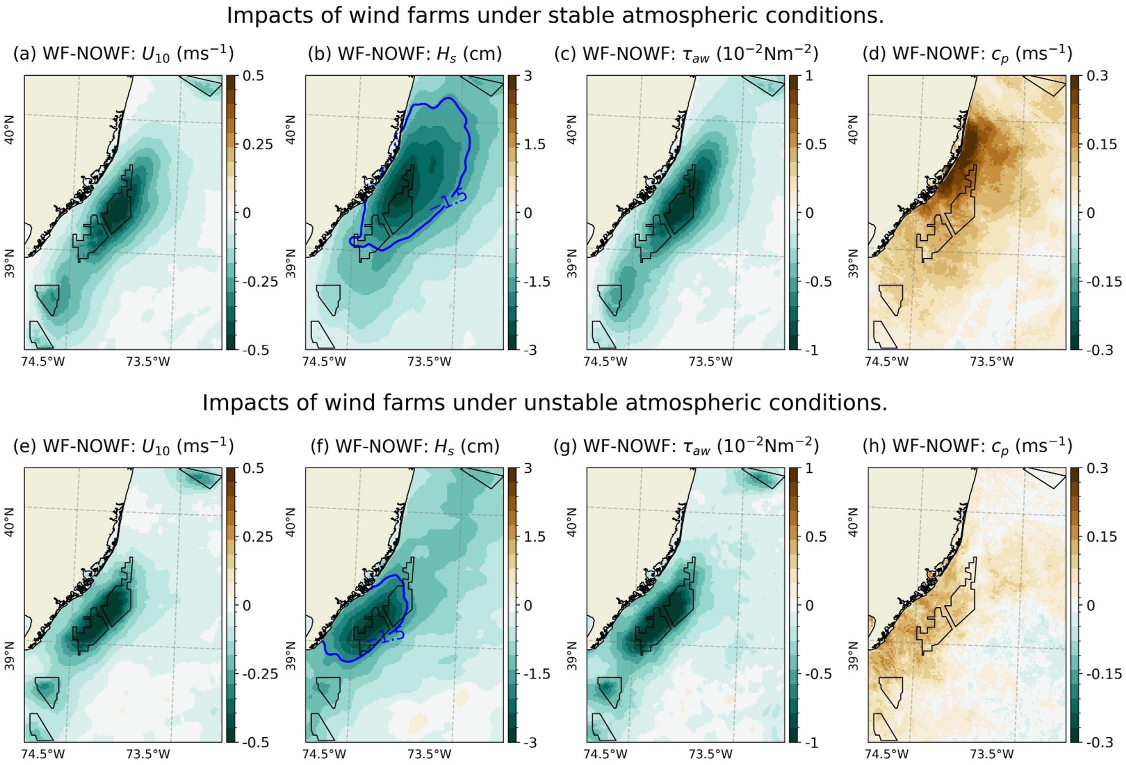

Figure 7. Same as Figure 6 but over NJ.

To quantitatively assess the changes in wave wakes under different atmospheric stability conditions, we define the wave wake extent as the area where H_s deficit exceeds 1.5%. This threshold is a tentatively chosen value to produce a wave wake scale comparable to that obtained using the commonly used 0.5 m s^{-1} wind speed deficit criterion used in wind wake studies. The relative differences remain essentially unchanged with different thresholds. At the New Jersey site, the wave wake during the stable conditions covers an area of approximately

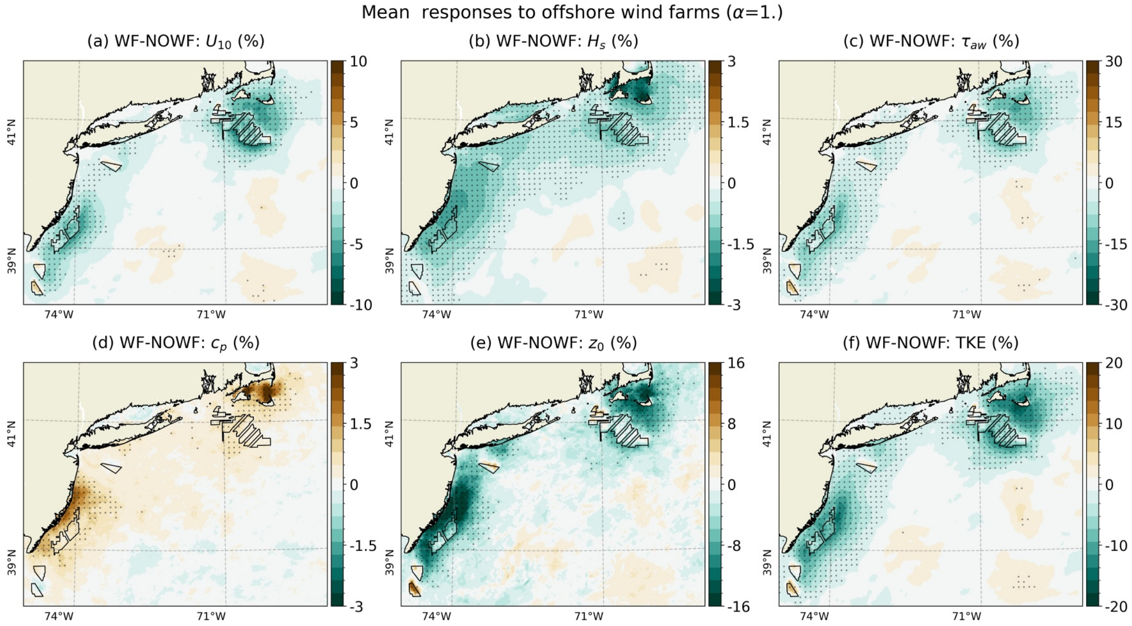

Figure 8. Similar to Figure 4 but using $\alpha = 1.0$.

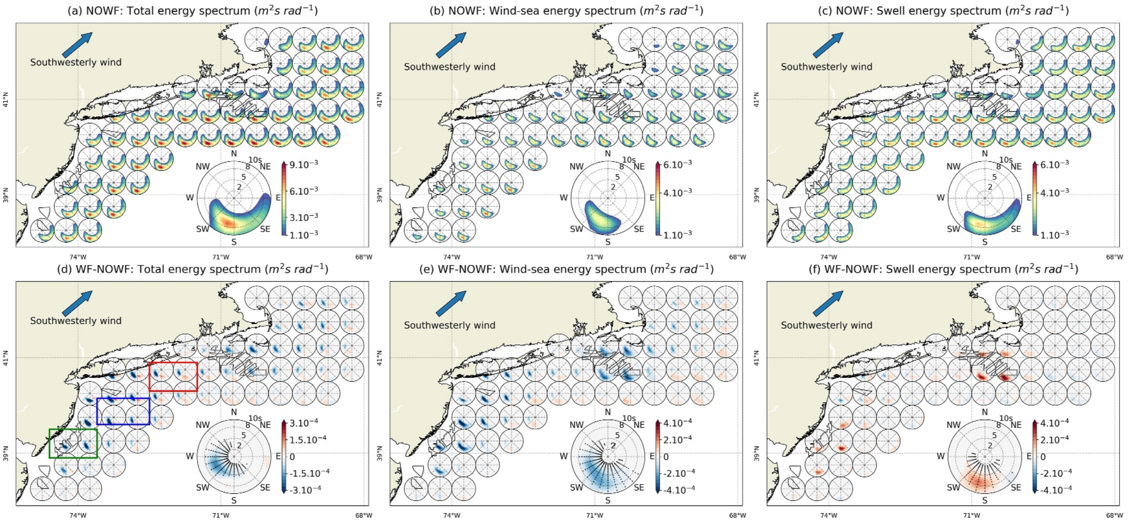

Figure 9. Southwesterly wind direction composite of the total wave energy spectrum in period space (m^2 s rad^{-1}) for (a) the unperturbed simulation NOWF. The averaged wave energy over the MA/RI lease area is represented by the main polar plot at the bottom of each panel. Wave energy spectra are plotted over the shelf where depth is between 15 and 500 m every 0.5∘ and are averaged over a 0.5∘ × 0.5∘ area. (b and c) Same as (a) but for (b) the wind-sea and (c) the swell component of the wave spectra. (d–f) Similar to (a–c) but for the directional wave energy spectrum differences WF-NOWF. Stippling on (d–f) represents the statistically significant responses at the 99% confidence level.

6,874 km^2, which decreases by a factor of 2.3–2,959 km^2 under unstable conditions (Figure 7). The larger extent of the wake during stable conditions is mainly associated with southwesterly conditions, whereas under unstable conditions, easterly to northeasterly winds dominate, and the coastline confines the wake extension (Figure 7).

At the MA/RI site, the opposite pattern occurs: the wave wake area increases from 7,148 km^2 in stable conditions to 9,988 km^2 in unstable conditions, about 1.4 times larger (Figure 6). This contrast arises because, under stable conditions, the southwesterly waves are partially blocked by Martha's Vineyard and Nantucket islands, limiting wake extension and development (Figure 6).

Atmospheric stability influences the spatial patterns of wave and sea state responses. However, the signs of these responses remain consistent regardless of stability. Both the all-stability composites (Figure 4) and the stability-based conditional composites (Figures 6 and 7) consistently show decreased H_s and τ_{aw} and increased c_p near the wind farms.

Regarding the effect of α value, results from WF_100 ($\alpha = 1.0$) (Figure 8) show considerably weaker responses in near-surface wind and wave variables than WF ($\alpha = 0.25$). In WF_100, changes in U_{10}, H_s, and τ_{aw} are minimal, or in some cases, slight increases are observed within the lease areas, especially under stable conditions. These findings are consistent with prior modeling studies of near-surface atmospheric and wave fields (Bodini et al., 2019; Larsén et al., 2024; Quint et al., 2024). Overall, the comparison between simulations across different α values shows consistent results. Therefore, for the remainder of this paper, we use the all-stability composites with $\alpha = 0.25$ as the baseline for analyzing changes in the spectral characteristics of surface waves.

3.2. Wave Energy Spectrum Responses

Using the output of directional wave spectra across the model domain, this section examines the changes in spectral characteristics and spatial distributions of the surface waves. Figures 9a and 9d show maps of the total wave energy density spectra for the unperturbed case (NOWF) and difference (WF-NOWF), respectively. These data are sampled over the shelf region, with water depths between 15 and 500 m. Wave energy spectra averaged over the MA/RI lease area are also displayed as enlarged directional wave spectra in the lower right corner of each panel. As in Figure 4, the stippling highlights the statistically significant differences.

This figure focuses on southwesterly wind conditions, which generate the bulk of the wind-wave energy in the southerly to southwesterly sectors (Figure 9a). Weak southeasterly waves are also present, but since these waves

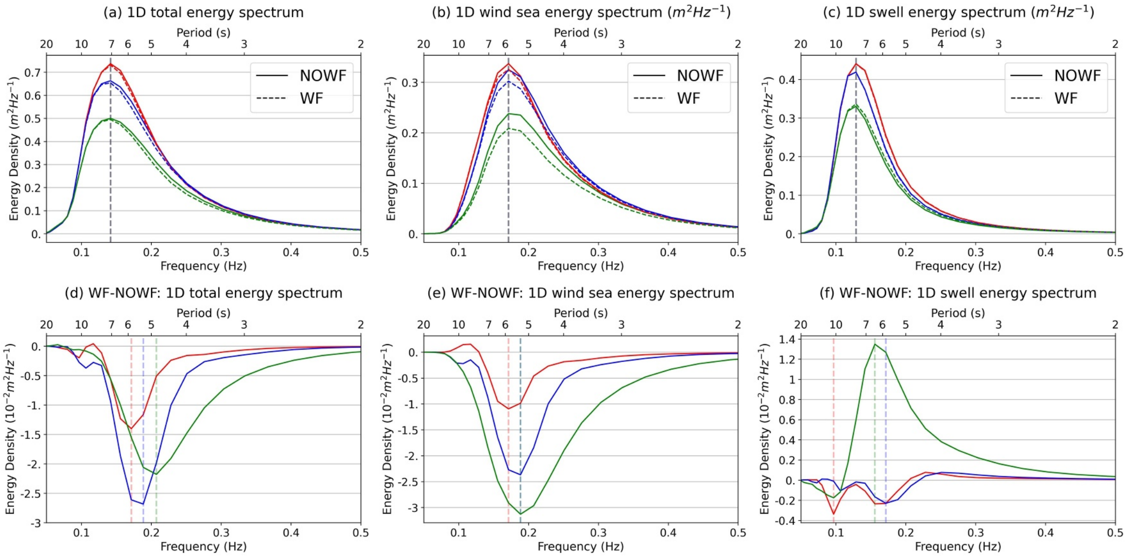

Figure 10. (a–c) 1-D total wave energy density (m^2 Hz^{-1}) of both NOWF (solid) and WF (dashed) averaged over the colored boxes located on Figure 9d for, respectively, (a) the total wave energy spectrum, (b) the wind sea, and (c) the swell component of the wave spectra. Each box corresponds to about 30 spectral points, and the frequency (period) of the energy peak is represented by the vertical line. (d–f) Similar to (a–c) but for the WF-NOWF 1-D differences in wave energy density. On (d–f), vertical lines represent the absolute peak difference values.

are not in the direction of the prevailing wind, they are interpreted as background swell. Similar directional spectral characteristics under northeasterly winds are presented in Figure S1 of the Supporting Information S1.

In response to wake-induced reductions in southwesterly U_{10}, wave energy decreases are most concentrated in the southwesterly sector, particularly at wave periods of around 5 s. In contrast, the southeasterly swell remains unaffected by the reduction in southwesterly U_{10} (Figure 9d).

To assess wave energy spectra responses as a function of fetch, three coast-parallel areas are selected and color-coded: the NJ lease area (green), the immediate wake region (blue), and the downstream and longer fetch region just southwest of the MA/RI lease areas (red). For each area, 1-D energy spectra in frequency space are calculated for NOWF (solid lines) and WF (dashed lines) in Figure 10a, and their differences (WF-NOWF) are shown in Figure 10d.

In all three regions, the total wave energy spectra peak at the swell frequency (7 s, Figure 10a), while the largest differences in wave energy between WF and NOWF occur at shorter periods. In the NJ lease area (green) and the immediate wake region (blue), wave energy reductions peak at 4.9–5.3 s, corresponding to wave energy decreases of approximately $2.1 \times 10^{-2} m^2$ Hz^{-1} (7%) and $2.6 \times 10^{-2} m^2$ Hz^{-1} (6%), respectively (Figures 9d and 10d). As the distance from the wind farm increases northeastward, in the red region with longer fetch, the spectral differences shift toward lower frequencies, peaking near 6 s and representing a smaller reduction of about $1.4 \times 10^{-2} m^2$ Hz^{-1} (2%) in wave energy (Figures 9d and 10d).

Using topographic partitions and a wave age cutoff (see Section 2.3), the total and difference in directional wave spectra are separated into wind-sea (Figures 9b and 9e) and swell (Figures 9c and 9f) components. Corresponding 1-D energy spectra are shown in Figures 10b, 10c, 10e, and 10f. Under dominant southwesterly wind conditions (Figures 9b and 10b), wind-sea energy peaks just below 6 s for all regions. Wind-sea energy is the lowest at the NJ lease area (green) compared to the downstream locations. This suggests the presence of fully developed waves in that region, as wave growth likely occurs upstream of the NJ lease area under southwesterly winds.

Under northeasterly winds, wind-sea energy and period increase with fetch, extending from the MA/RI lease area downstream (Figures S1 and S2 in Supporting Information S1). This behavior is more consistent with the wave age-dependent fetch laws, which describe how wind-seas grow in the direction of the prevailing wind (i.e., Hasselmann et al., 1973; Kahma & Calkoen, 1992; Young, 1997).

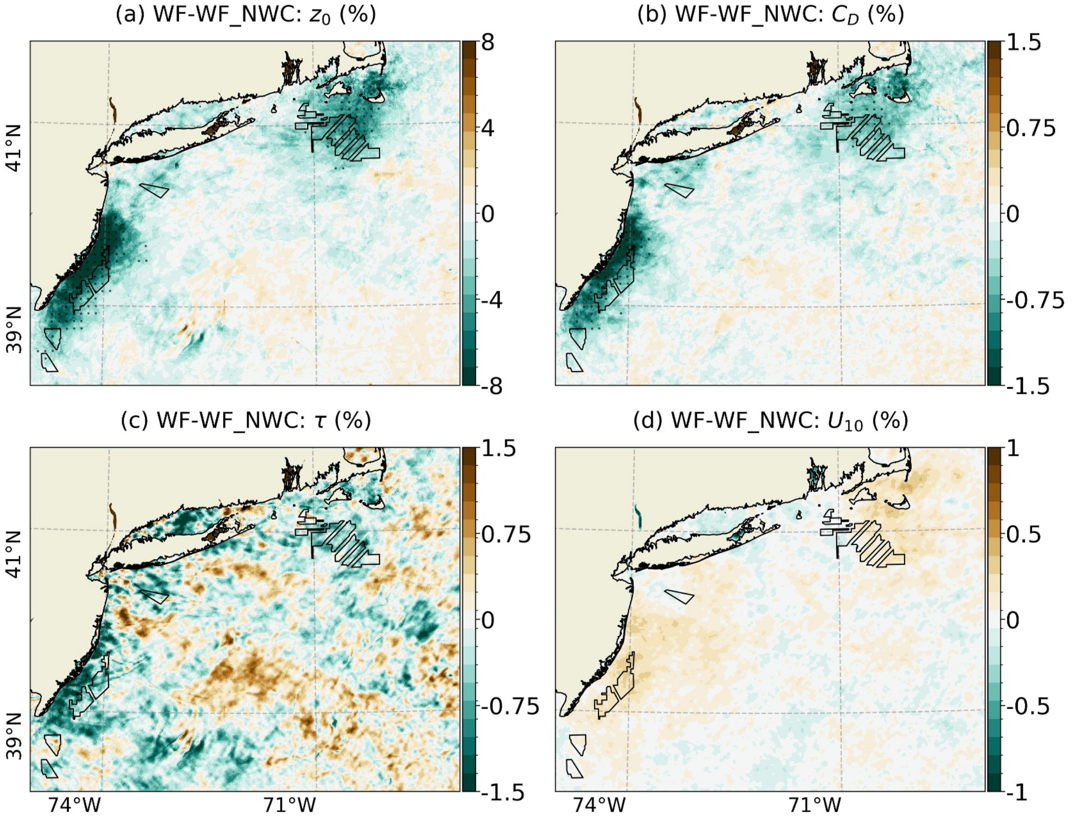

Figure 11. Time-averaged (JJA, 2017–2021) differences WF − WF_NWC in percent for (a) ocean surface roughness length (z_0), (b) drag coefficient (C_D), (c) surface wind stress (τ), and (d) 10 m wind speed (U_{10}). Statistically significant responses at the 99% confidence level are marked with gray dots.

The wind-sea component, typically consisting of shorter waves aligned with the prevailing wind, shows the most significant reduction in energy density within the wind farm region (green) with a $3.1 \times 10^{-2} \mathrm{m}^2\ \mathrm{Hz}^{-1}$ (13%) decrease (Figures 9e and 10e). Smaller reductions are observed in the immediate wake region (blue), with $2.4 \times 10^{-2} \mathrm{m}^2\ \mathrm{Hz}^{-1}$ (8%) and $1 \mathrm{x} 10^{-2} \mathrm{m}^2\ \mathrm{Hz}^{-1}$ (3%) for region with longer fetch (red). These results are consistent with previous findings that wind farms reduce wave energy and that the reduction is fetch-dependent (Bärfuss et al., 2021; Larsén et al., 2024). Similar wind-sea energy decrease is found in the case of northeasterly winds (Figures S1 and S2 in Supporting Information S1).

The swell component exhibits broader directional spreading, ranging from southwest to southeast (Figure 9c). Swell wave energy originating from directions not aligned with prevailing wind remains unchanged (Figure 9f), as these waves are likely generated outside the model domain and are unaffected by wind speed reductions induced by the wind farms.

In contrast, swell wave energy aligned with the prevailing wind increases within the NJ and MA/RI lease areas (Figures 9f and 10f). This increase corresponds to a local reduction in wind-sea energy (green box, Figures 9e, 9f, 10e, and 10f). The shift in wave energy to lower frequencies occurs because wind waves generated upstream of the NJ and MA/RI lease areas become "swell-like," as they enter regions where near-surface wind speeds decrease due to the presence of wind farm wakes (Figure 4). This results in a transition in sea state from a fully developed wind-sea regime to a swell-dominated regime. The transition is most pronounced under southerly wind conditions, where longer fetch allows wind seas to develop upstream of the wind farms. It is less evident under fetch-limited conditions, such as northerly to westerly winds (not shown). The shift toward longer-period waves is consistent with the observed increase in peak phase speed (c_p) (Figure 4d).

Overall, wind farms induce broad spectral modifications to sea states across varying fetches. Most of the total wave energy reductions occur in the wind-sea component, with a partially compensating increase in swell energy near the lease areas, particularly when the swell is in the direction of the prevailing wind. As fetch increases, short wind waves continue to weaken within wind wakes but without a corresponding increase in swell energy. This leads to the maximum wave energy reductions in the immediate wake region of the NJ lease area (blue, Figure 10e).

In WW3, we used the source term 4 (ST4, Ardhuin et al., 2010) package, which represents energy transfer from wind to waves, leading to wave growth. Wind input in ST4 depends on the wind-wave growth rate, γ, which, according to the quasi-linear theory of wind-wave generation (Janssen, 1991), scales with the squared inverse wave age, expressed as

$$\gamma = \epsilon\beta\omega\left(\frac{u_*}{c}\right)^2 \cos^2\theta. \tag{3}$$

Here, ϵ denotes the air-sea density ratio, ω the angular frequency, c the phase speed, θ the wave propagation angle, and the Miles parameter β, which also depends on the inverse wave age.

Since wind wakes reduce τ_{aw} and consequently u_* while increasing c_p, these changes collectively result in a lower inverse wave age, thereby reducing wind input and the wind-wave growth rate.

It is worth noting that this wind-wave growth parameterization assumes a logarithmic velocity profile in the atmospheric boundary layer. While wind farms can disrupt this profile, the parameterization may remain applicable if the boundary layer quickly adjusts to turbine wakes or if deviations occur above the critical layer heights. A complete assessment of these effects on wind-wave growth mechanisms falls beyond the focus of this study but may be valuable for future investigation.

3.3. Isolating Wave Impacts on Surface Drag

The decrease in inverse wave age and H_s has implications for air-sea momentum exchange and surface drag. This is because many modern bulk air-sea flux parameterizations define roughness length as a function of inverse wave age and/or wave slope (e.g., Drennan et al., 2005; Edson et al., 2013; Sauvage et al., 2023; Taylor & Yelland, 2001). In this study, we employ the wave age and wave slope-dependent formulation of Edson et al. (2013), as described in Equation 1.

This section quantifies the changes in z_0, C_d, and τ caused by the reductions in inverse wave age and H_s reported in the previous section using additional WRF-only simulations (WF_NWC). In WF_NWC, the wind farm parameterization is switched on, but sea state is prescribed from NOWF simulations; hence, the sea state input to Equation 1 has been unaffected by wind wakes and corresponds to unperturbed states. Sea surface temperature and ocean surface currents are identical between WF_NWC and WF. Therefore, any difference in the atmospheric outputs can be attributed solely to sea state changes via c_p and H_s (Figures 4b and 4d), independent of bulk atmospheric variables.

Figure 11 shows the average percentage differences between WF and WF_NWC in z_0, C_D, τ, and U_{10}. Compared to the 20% decrease in z_0 shown previously in Figure 4e, Figure 11a shows a 5 %–8% decrease in z_0. This suggests that roughly one-third of the z_0 reductions shown in Figure 4e is attributable to changes in c_p and H_s, while the remaining two-thirds result from the decrease in friction velocity (u_*). These wave-induced changes in z_0 lead to modest reductions in C_D and τ, on the order of 1%–2% (Figures 11b and 11c). A collocated, but even smaller increase in U_{10} is also observed, averaging less than 0.5% (Figure 11d).

The results shown in Figure 11 are consistent with the sea state changes shown in Figures 4b and 4d. Overall, the magnitude of changes is small, except for z_0. These results indicate that the influence of sea state changes on the drag coefficient and wind stress is secondary to the dominant effect of reduced friction velocity due to lower wind speeds.

4. Conclusion

This study investigates the response of sea state to offshore wind farms in the coastal ocean of the northeast U.S. using fully coupled ocean-atmosphere-wave model simulations with and without wind farm wake parameterization. Consistent with previous studies (i.e., Bodini et al., 2021; Larsén et al., 2024; Quint et al., 2024), our results show that turbine-induced wind wakes cause a significant reduction in near-surface wind speeds near the wind farms (approximately 10%). This wind speed reduction leads to a corresponding decrease in significant wave height (by about 3%) and wave-supported stress (by approximately 30%).

Consistent with Quint et al. (2024), we find that wake-induced wind reductions extend further downstream under stable atmospheric conditions, whereas under unstable conditions, wind deficits remain largely confined to the lease areas, with minimal downstream propagation. Although the magnitude, and in some cases even the sign, of the response may vary under specific conditions (e.g., stable and $\alpha = 1.0$), the overall comparison across simulations with different α values yields consistent results. This suggests that the simulated changes in near-surface wind and surface wave fields (Figure 4) are robust to the choice of α.

Spectral analysis reveals a reduction in the wind-sea component of wave energy within the wake regions, indicating suppressed local wind-wave growth. This reduction in short wind waves leads to lower surface roughness length, wind stress, and ocean surface turbulent kinetic energy, likely diminishing near-surface ocean mixing.

Additionally, the reduced surface wind speed and wind-to-wave energy result in an average increase of approximately 3% in the peak wave phase speed near the wind farms, indicating a shift toward higher wave age and an older sea state. This shift occurs because fully developed waves generated upstream of the wind farms begin to outrun the locally weakened winds within the lease areas. The transition toward a swell-dominated regime is most pronounced under southwesterly winds, which support longer fetch and sustained wave growth, and is less evident under northerly to westerly winds, where fetch is limited.

We demonstrate that wind farms reduce wind speed, and consequently, wind stress and friction velocity, while increasing peak wave speed, resulting in a lower inverse wave age. At the same time, the reduction in significant wave height lowers the wave slope. Together, these changes in wind and wave characteristics contribute to a reduction in surface roughness length (Figure 4e).

To isolate the role of sea state feedback in modifying surface drag, we performed additional WRF-only simulations, in which sea state is prescribed from unperturbed simulations (NOWF). Results show that the primary driver of wind stress reduction in the presence of wind farms is the wake-induced wind speed deficit, rather than changes in sea states.

The sea state changes examined in this study ultimately result in a reduction of mean wave energy flux or wave power, which depends on both significant wave height and the mean wave period. On average, during summer, wave power may decrease by about 3% (0.12 kW m^{-1}) (not shown). Such systematic reductions in coastal wave power could potentially have implications for nearshore dynamics, including changes in coastal erosion patterns and sediment transport processes. While these coastal impacts lie beyond the scope of the present study, they represent important directions for future research.

Further research is needed to assess the long-term effects of offshore wind farms on regional wind and wave climates, as well as on upper-ocean processes. These findings are important not only for advancing our understanding of the complex interactions occurring within turbine wakes but also for informing robust environmental assessments near wind farm installations. The responses identified in this study are likely modulated by multiple factors not considered in this study, including variations in turbine locations, layouts, and sizes, as well as potential interactions among neighboring wind farms. Comprehensive, high-resolution coupled modeling studies that systematically assess these factors are crucial for guiding the effective and sustainable design, siting, and operation of offshore wind energy projects in a manner that mitigates unintended impacts on the coastal environment.

Conflict of Interest

The authors declare no conflicts of interest relevant to this study.

Data Availability Statement

ERA5 data are made available by Copernicus Climate Change Service https://cds.climate.copernicus.eu), Mercator by Copernicus Marine Environment Monitoring Service (CMEMS, 2024), global 3-hourly spectral wave analyses by Ifremer (ftp://ftp.ifremer.fr/ifremer/ww3/HINDCAST/GLOBAL, and National Data Buoy Center (NDBC) buoy data at https://www.ndbc.noaa.gov. The SCOAR coupler code and tutorials are accessible via the GitHub repository (https://github.com/SCOAR-model). The original COARE3.5 algorithm can be found at https://github.com/NOAA-PSL/COARE-algorithm while the modified COARE3.5 codes (Sauvage et al., 2023, 2024) used in this study can be accessed through Zenodo (Sauvage, 2025). Python codes used to generate the figures and input files for WRF, ROMS, and WW3, including those to run the Fitch wind farm parameterization in WRF (Rosencrans et al., 2024), are also provided through Zenodo (Sauvage et al., 2025). The "Wavespectra" Python library is available on GitHub at https://github.com/wavespectra/wavespectra.

Acknowledgments

The authors acknowledge support from the U.S. Department of Energy (DOE) under DE-EE0009424. H.S. is grateful for support from NASA (80NSSC21K1524), NSF (OCE-2148120, OCE-2022846), NOAA (NA19OAR4310376, NA22OAR4310598), and the Uehiro Center for the Advancement of Oceanography (UC·AO) at the University of Hawai'i at Mānoa. S.Z. is grateful for support from NASA (80NSSC21K0832) and NSF (2023020, 2316818). The computational resources were provided by the National Renewable Energy Laboratory's (NREL) high-performance computing system.

References

Akhtar, N., Geyer, B., Rockel, B., Sommer, P. S., & Schrum, C. (2021). Accelerating deployment of offshore wind energy alter wind climate and reduce future power generation potentials. *Scientific Reports*, *11*(1), 11826. https://doi.org/10.1038/s41598-021-91283-3

Akhtar, N., Geyer, B., & Schrum, C. (2022). Impacts of accelerating deployment of offshore windfarms on near-surface climate. *Scientific Reports*, *12*(1), 18307. https://doi.org/10.1038/s41598-022-22868-9

Alari, V., & Raudsepp, U. (2012). Simulation of wave damping near coast due to offshore wind farms. *Journal of Coastal Research*, *28*(1), 143–148. https://doi.org/10.2112/JCOASTRES-D-10-00054.1

Ali, K., Schultz, D. M., Revell, A., Stallard, T., & Ouro, P. (2023). Assessment of five wind-farm parameterizations in the weather research and forecasting model: A case study of wind farms in the North Sea. *Monthly Weather Review*, *151*(9), 2333–2359. https://doi.org/10.1175/MWR-D-23-0006.1

AlSam, A., Szasz, R., & Revstedt, J. (2015). The influence of sea waves on offshore wind turbine aerodynamics. *Journal of Energy Resources Technology*, *137*, 051209. https://doi.org/10.1115/1.4031005

Archer, C. L., Wu, S., Ma, Y., & Jiménez, P. A. (2020). Two corrections for turbulent kinetic energy generated by wind farms in the WRF model. *Monthly Weather Review*, *148*(12), 4823–4835. https://doi.org/10.1175/MWR-D-20-0097.1

Ardhuin, F., Chapron, B., & Collard, F. (2009). Observation of swell dissipation across oceans. *Geophysical Research Letters*, *36*(6), 2008GL037030. https://doi.org/10.1029/2008GL037030

Ardhuin, F., O'Reilly, W. C., Herbers, T. H. C., & Jessen, P. F. (2003). Swell transformation across the continental shelf. Part I: Attenuation and directional broadening. *Journal of Physical Oceanography*, *33*(9), 1921–1939. https://doi.org/10.1175/1520-0485(2003)033⟨1921:STATCS⟩2.0.CO;2

Ardhuin, F., Rogers, E., Babanin, A. V., Filipot, J.-F., Magne, R., Roland, A., et al. (2010). Semiempirical dissipation source functions for ocean waves. Part I: Definition, calibration, and validation. *Journal of Physical Oceanography*, *40*(9), 1917–1941. https://doi.org/10.1175/2010JPO4324.1

Ardhuin, F., & Roland, A. (2012). Coastal wave reflection, directional spread, and seismoacoustic noise sources. *Journal of Geophysical Research*, *117*(C11), C00J20. https://doi.org/10.1029/2011JC007832

Bärfuss, K., Schulz-Stellenfleth, J., & Lampert, A. (2021). The impact of offshore wind farms on sea state demonstrated by airborne LiDAR measurements. *Journal of Marine Science and Engineering*, *9*(6), 644. https://doi.org/10.3390/jmse9060644

Battjes, J. A., & Janssen, J. P. F. M. (1978). Energy loss and set-up due to breaking of random waves. *Coastal Engineering*, 569–587. https://doi.org/10.1061/9780872621909.034

Benkort, D., Christiansen, N., Ho-Hagemann, H. T. M., Daewel, U., & Gilles, A. (2024). How do offshore wind farms affect the ocean? *Frontiers for Young Minds*, *12*, 1336535. https://doi.org/10.3389/frym.2024.1336535

Bodini, N., Lundquist, J. K., & Kirincich, A. (2019). U.S. East Coast LiDAR measurements show offshore wind turbines will encounter very low atmospheric turbulence. *Geophysical Research Letters*, *46*(10), 5582–5591. https://doi.org/10.1029/2019GL082636

Bodini, N., Lundquist, J. K., & Moriarty, P. (2021). Wind plants can impact long-term local atmospheric conditions. *Scientific Reports*, *11*(1), 22939. https://doi.org/10.1038/s41598-021-02089-2

Bretherton, C. S., Widmann, M., Dymnikov, V. P., Wallace, J. M., & Bladé, I. (1999). The effective number of spatial degrees of freedom of a time-varying field. *Journal of Climate*, *12*(7), 1990–2009. https://doi.org/10.1175/1520-0442(1999)012⟨1990:TENOSD⟩2.0.CO;2

Broström, G. (2008). On the influence of large wind farms on the upper ocean circulation. *Journal of Marine Systems*, *74*(1), 585–591. https://doi.org/10.1016/j.jmarsys.2008.05.001

Canuto, V. M., Howard, A., Cheng, Y., & Dubovikov, M. S. (2001). Ocean turbulence. Part I: One-point closure model—Momentum and heat vertical diffusivities. *Journal of Physical Oceanography*, *31*(6), 1413–1426. https://doi.org/10.1175/1520-0485(2001)031⟨1413:OTPIOP⟩2.0.CO;2

Carpenter, J. R., Merckelbach, L., Callies, U., Clark, S., Gaslikova, L., & Baschek, B. (2016). Potential impacts of offshore wind farms on North Sea stratification. *PLoS One*, *11*(8), e0160830. https://doi.org/10.1371/journal.pone.0160830

Christensen, E. D., Kristensen, S. E., & Deigaard, R. (2014). Impact of an offshore wind farm on wave conditions and shoreline development. *Coastal Engineering Proceedings*, *1*(34), 87. https://doi.org/10.9753/icce.v34.sediment.87

Christiansen, N., Carpenter, J. R., Daewel, U., Suzuki, N., & Schrum, C. (2023). The large-scale impact of anthropogenic mixing by offshore wind turbine foundations in the shallow North Sea. *Frontiers in Marine Science*, *10*, 1178330. https://doi.org/10.3389/fmars.2023.1178330

Christiansen, N., Daewel, U., Djath, B., & Schrum, C. (2022). Emergence of large-scale hydrodynamic structures due to atmospheric offshore wind farm wakes. *Frontiers in Marine Science*, *9*, 818501. https://doi.org/10.3389/fmars.2022.818501

Christiansen, N., Daewel, U., & Schrum, C. (2022). Tidal mitigation of offshore wind wake effects in coastal seas. *Frontiers in Marine Science*, *9*, 1006647. https://doi.org/10.3389/fmars.2022.1006647

CMEMS. (2024). Global ocean physics analysis and forecast [Dataset]. *E.U. Copernicus Marine Service Information (CMEMS). Marine Data Store (MDS)*. https://doi.org/10.48670/moi-00016

Daewel, U., Akhtar, N., Christiansen, N., & Schrum, C. (2022). Offshore wind farms are projected to impact primary production and bottom water deoxygenation in the North Sea. *Communications Earth & Environment*, *3*(1), 1–8. https://doi.org/10.1038/s43247-022-00625-0

Deskos, G., Lee, J. C. Y., Draxl, C., & Sprague, M. A. (2021). Review of wind–wave coupling models for large-eddy simulation of the marine atmospheric boundary layer. *Journal of the Atmospheric Sciences*, *78*(10), 3025–3045. https://doi.org/10.1175/JAS-D-21-0003.1

Dorrell, R. M., Lloyd, C. J., Lincoln, B. J., Rippeth, T. P., Taylor, J. R., Caulfield, C.-C. P., et al. (2022). Anthropogenic mixing in seasonally stratified shelf seas by offshore wind farm infrastructure. *Frontiers in Marine Science*, *9*, 830927. https://doi.org/10.3389/fmars.2022.830927

Drennan, W. M., Taylor, P. K., & Yelland, M. J. (2005). Parameterizing the sea surface roughness. *Journal of Physical Oceanography*, *35*(5), 835–848. https://doi.org/10.1175/JPO2704.1

Edson, J. B., Jampana, V., Weller, R. A., Bigorre, S. P., Plueddemann, A. J., Fairall, C. W., et al. (2013). On the exchange of momentum over the open ocean. *Journal of Physical Oceanography*, *43*(8), 1589–1610. https://doi.org/10.1175/JPO-D-12-0173.1

Egbert, G. D., & Erofeeva, S. Y. (2002). Efficient inverse modeling of barotropic ocean tides. *Journal of Atmospheric and Oceanic Technology*, *19*(2), 183–204. https://doi.org/10.1175/1520-0426(2002)019⟨0183:EIMOBO⟩2.0.CO;2

Fairall, C. W., Bradley, E. F., Hare, J. E., Grachev, A. A., & Edson, J. B. (2003). Bulk parameterization of air–sea fluxes: Updates and verification for the COARE algorithm. *Journal of Climate*, *16*(4), 571–591. https://doi.org/10.1175/1520-0442(2003)016⟨0571:BPOASF⟩2.0.CO;2

Fairall, C. W., Bradley, E. F., Rogers, D. P., Edson, J. B., & Young, G. S. (1996). Bulk parameterization of air-sea fluxes for tropical ocean-global atmosphere coupled-ocean atmosphere response experiment. *Journal of Geophysical Research*, *101*(C2), 3747–3764. https://doi.org/10.1029/95JC03205

Fischereit, J., Brown, R., Larsén, X. G., Badger, J., & Hawkes, G. (2022). Review of mesoscale wind-farm parametrizations and their applications. *Boundary-Layer Meteorology*, *182*(2), 175–224. https://doi.org/10.1007/s10546-021-00652-y

Fischereit, J., Larsén, X. G., & Hahmann, A. N. (2022). Climatic impacts of wind-wave-wake interactions in offshore wind farms. *Frontiers in Energy Research*, *10*, 881459. https://doi.org/10.3389/fenrg.2022.881459

Fitch, A. C., Olson, J. B., Lundquist, J. K., Dudhia, J., Gupta, A. K., Michalakes, J., & Barstad, I. (2012). Local and mesoscale impacts of wind farms as parameterized in a mesoscale NWP model. *Monthly Weather Review*, *140*(9), 3017–3038. https://doi.org/10.1175/MWR-D-11-00352.1

Floeter, J., Pohlmann, T., Harmer, A., & Möllmann, C. (2022). Chasing the offshore wind farm wind-wake-induced upwelling/downwelling dipole. *Frontiers in Marine Science*, *9*, 884943. https://doi.org/10.3389/fmars.2022.884943

Golbazi, M., & Archer, C. L. (2019). Methods to estimate surface roughness length for offshore wind energy. *Advances in Meteorology*, *2019*(1), 5695481. https://doi.org/10.1155/2019/5695481

Golbazi, M., Archer, C. L., & Alessandrini, S. (2022). Surface impacts of large offshore wind farms. *Environmental Research Letters*, *17*(6), 064021. https://doi.org/10.1088/1748-9326/ac6e49

Haidvogel, D. B., Arango, H. G., Hedstrom, K., Beckmann, A., Malanotte-Rizzoli, P., & Shchepetkin, A. F. (2000). Model evaluation experiments in the North Atlantic Basin: Simulations in nonlinear terrain-following coordinates. *Dynamics of Atmospheres and Oceans*, *32*(3), 239–281. https://doi.org/10.1016/S0377-0265(00)00049-X

Hanson, J. L., & Phillips, O. M. (2001). Automated analysis of ocean surface directional wave spectra. *Journal of Atmospheric and Oceanic Technology*, *18*(2), 277–293. https://doi.org/10.1175/1520-0426(2001)018⟨0277:AAOOSD⟩2.0.CO;2

Hanson, J. L., Tracy, B. A., Tolman, H. L., & Scott, R. D. (2009). Pacific hindcast performance of three numerical wave models. *Journal of Atmospheric and Oceanic Technology*, *26*(8), 1614–1633. https://doi.org/10.1175/2009JTECHO650.1

Hasselmann, K., Barnett, T. P., Bouws, E., Carlson, H., Cartwright, D. E., Enke, K., et al. (1973). Measurements of wind-wave growth and swell decay during the joint North Sea wave project (JONSWAP). *Ergänzungsheft zur Deutschen Hydrographischen Zeitschrift, Reihe A, Nr. 12*.

Hersbach, H., Bell, B., Berrisford, P., Hirahara, S., Horányi, A., Muñoz-Sabater, J., et al. (2020). The ERA5 global reanalysis. *Quarterly Journal of the Royal Meteorological Society*, *146*(730), 1999–2049. https://doi.org/10.1002/qj.3803

Hosseini, S. T., Pein, J., Staneva, J., Zhang, Y. J., & Stanev, E. (2025). Impact of offshore wind farm monopiles on hydrodynamics interacting with wind-driven waves. *Ocean Modelling*, *195*, 102521. https://doi.org/10.1016/j.ocemod.2025.102521

Iacono, M. J., Delamere, J. S., Mlawer, E. J., Shephard, M. W., Clough, S. A., & Collins, W. D. (2008). Radiative forcing by long-lived greenhouse gases: Calculations with the AER radiative transfer models. *Journal of Geophysical Research*, *113*(D13), D13103. https://doi.org/10.1029/2008JD009944

Janssen, P. A. E. M. (1991). Quasi-linear theory of wind-wave generation applied to wave forecasting. *Journal of Physical Oceanography*, *21*(11), 1631–1642. https://doi.org/10.1175/1520-0485(1991)021<1631:qltoww>2.0.co;2

Kahma, K. K., & Calkoen, C. J. (1992). Reconciling discrepancies in the observed growth of wind-generated waves. *Journal of Physical Oceanography*, *22*(12), 1389–1405. https://doi.org/10.1175/1520-0485(1992)022⟨1389:RDITOG⟩2.0.CO;2

Kain, J. S. (2004). The Kain–Fritsch convective parameterization: An update. *Journal of Applied Meteorology*, *43*(1), 170–181. https://doi.org/10.1175/1520-0450(2004)043⟨0170:TKCPAU⟩2.0.CO;2

Kalvig, S., Manger, E., Hjertager, B. H., & Jakobsen, J. B. (2014). Wave influenced wind and the effect on offshore wind turbine performance. *Energy Procedia*, *53*, 202–213. https://doi.org/10.1016/j.egypro.2014.07.229

Larsén, X. G., & Fischereit, J. (2021). A case study of wind farm effects using two wake parameterizations in the Weather Research and Forecasting (WRF) model (V3.7.1) in the presence of low-level jets. *Geoscientific Model Development*, *14*(6), 3141–3158. https://doi.org/10.5194/gmd-14-3141-2021

Larsén, X. G., Fischereit, J., Hamzeloo, S., Bärfuss, K., & Lampert, A. (2024). Investigation of wind farm impacts on surface waves using coupled numerical simulations. *Renewable Energy*, *237*, 121671. https://doi.org/10.1016/j.renene.2024.121671

Lellouche, J.-M., Greiner, E., Le Galloudec, O., Garric, G., Regnier, C., Drevillon, M., et al. (2018). Recent updates to the Copernicus Marine Service global ocean monitoring and forecasting real-time 1/12° high-resolution system. *Ocean Science*, *14*(5), 1093–1126. https://doi.org/10.5194/os-14-1093-2018

Ludewig, E. (2015). *On the effect of offshore wind farms on the atmosphere and ocean dynamics* (No. 31). Springer. https://doi.org/10.1007/978-3-319-08641-5

McCombs, M. P., Mulligan, R. P., & Boegman, L. (2014). Offshore wind farm impacts on surface waves and circulation in Eastern Lake Ontario. *Coastal Engineering*, *93*, 32–39. https://doi.org/10.1016/j.coastaleng.2014.08.001

Monin, A. S., & Obukhov, A. M. (1954). *Basic laws of turbulent mixing in the surface layer of the atmosphere* (Vol. 24(151), pp. 163–187). Trudy Geofiz, Instituta Akademii Nauk, SSSR.

Nakanishi, M., & Niino, H. (2009). Development of an improved turbulence closure model for the atmospheric boundary layer. *Journal of the Meteorological Society of Japan. Series II*, *87*(5), 895–912. https://doi.org/10.2151/jmsj.87.895

Ning, X., & Paskyabi, M. B. (2024). Parameterization of wave-induced stress in large-eddy simulations of the marine atmospheric boundary layer. *Journal of Geophysical Research: Oceans*, *129*(9), e2023JC020722. https://doi.org/10.1029/2023JC020722

Ning, X., Paskyabi, M. B., Bui, H. H., & Penchah, M. M. (2023). Evaluation of sea surface roughness parameterization in meso-to-micro scale simulation of the offshore wind field. *Journal of Wind Engineering and Industrial Aerodynamics*, *242*, 105592. https://doi.org/10.1016/j.jweia.2023.105592

Olson, J. B., Kenyon, J. S., Angevine, W. A., Brown, J. M., Pagowski, M., & Sušelj, K. (2019). A description of the MYNN-EDMF scheme and the coupling to other components in WRF–ARW. https://doi.org/10.25923/N9WM-BE49

Olson, J. B., Smirnova, T., Kenyon, J. S., Turner, D. D., Brown, J. M., Zheng, W., & Green, B. W. (2021). A description of the MYNN surface-layer scheme. In *NOAA Technical Memorandum OAR GSL*. https://doi.org/10.25923/F6A8-BC75

Paskyabi, M. B., & Fer, I. (2012). Upper ocean response to large wind farm effect in the presence of surface gravity waves. *Energy Procedia*, *24*, 245–254. https://doi.org/10.1016/j.egypro.2012.06.106

Ponce de León, S., Bettencourt, J. H., & Kjerstad, N. (2011). Simulation of irregular waves in an offshore wind farm with a spectral wave model. *Continental Shelf Research*, *31*(15), 1541–1557. https://doi.org/10.1016/j.csr.2011.07.003

Porchetta, S., Muñoz-Esparza, D., Munters, W., van Beeck, J., & van Lipzig, N. (2021). Impact of ocean waves on offshore wind farm power production. *Renewable Energy*, *180*, 1179–1193. https://doi.org/10.1016/j.renene.2021.08.111

Porchetta, S., Temel, O., Warner, J., Muñoz-Esparza, D., Monbaliu, J., Van Beeck, J., & Van Lipzig, N. (2021). Evaluation of a roughness length parametrization accounting for wind–wave alignment in a coupled atmosphere–wave model. *Quarterly Journal of the Royal Meteorological Society*, *147*(735), 825–846. https://doi.org/10.1002/qj.3948

Portilla, J., Ocampo-Torres, F. J., & Monbaliu, J. (2009). Spectral partitioning and identification of wind sea and swell. *Journal of Atmospheric and Oceanic Technology*, *26*(1), 107–122. https://doi.org/10.1175/2008JTECHO609.1

Quint, D., Lundquist, J. K., Bodini, N., & Rosencrans, D. (2024). Meteorological impacts of offshore wind turbines as simulated in the weather research and forecasting model. *Wind Energy Science Discussions*, 1–34. https://doi.org/10.5194/wes-2024-53

Quint, D., Lundquist, J. K., & Rosencrans, D. (2025). Simulations suggest offshore wind farms modify low-level jets. *Wind Energy Science*, *10*(1), 117–142. https://doi.org/10.5194/wes-10-117-2025

Raghukumar, K., Chartrand, C., Chang, G., Cheung, L., & Roberts, J. (2022). Effect of floating offshore wind turbines on atmospheric circulation in California. *Frontiers in Energy Research*, *10*, 863995. https://doi.org/10.3389/fenrg.2022.863995

Rascle, N., & Ardhuin, F. (2013). A global wave parameter database for geophysical applications. Part 2: Model validation with improved source term parameterization. *Ocean Modelling*, *70*, 174–188. https://doi.org/10.1016/j.ocemod.2012.12.001

Rosencrans, D., Lundquist, J. K., Optis, M., Rybchuk, A., Bodini, N., & Rossol, M. (2024). Seasonal variability of wake impacts on US mid-Atlantic offshore wind plant power production. *Wind Energy Science*, *9*(3), 555–583. https://doi.org/10.5194/wes-9-555-2024

Sauvage, C. (2025). COARE3.5 wave-based code, Sauvage et al. v1.0 [Dataset]. *Zenodo*. https://doi.org/10.5281/zenodo.17547039

Sauvage, C., Seo, H., Barr, B. W., Edson, J. B., & Clayson, C. A. (2024). Misaligned wind-waves behind atmospheric cold fronts. *Journal of Geophysical Research: Oceans*, *129*(9), e2024JC021162. https://doi.org/10.1029/2024JC021162

Sauvage, C., Seo, H., Clayson, C. A., & Edson, J. B. (2023). Improving wave-based air-sea momentum flux parameterization in mixed seas. *Journal of Geophysical Research: Oceans*, *128*(3), e2022JC019277. https://doi.org/10.1029/2022JC019277

Sauvage, C., Seo, H., Zippel, S., Clayson, C. A., & Edson, J. B. (2025). Dataset for sauvage et al.: "fetch-dependent surface wave responses to offshore wind farms in the northeast U.S. Coast" [Dataset]. *Zenodo*. https://doi.org/10.5281/zenodo.15793972

Schultze, L. K. P., Merckelbach, L. M., Horstmann, J., Raasch, S., & Carpenter, J. R. (2020). Increased mixing and turbulence in the wake of offshore wind farm foundations. *Journal of Geophysical Research: Oceans*, *125*(8), e2019JC015858. https://doi.org/10.1029/2019JC015858

Seo, H., Miller, A. J., & Roads, J. O. (2007). The Scripps Coupled Ocean–Atmosphere Regional (SCOAR) model, with applications in the Eastern Pacific sector. *Journal of Climate*, *20*(3), 381–402. https://doi.org/10.1175/JCLI4016.1

Shchepetkin, A. F., & McWilliams, J. C. (2005). The regional oceanic modeling system (ROMS): A split-explicit, free-surface, topography-following-coordinate oceanic model. *Ocean Modelling*, *9*(4), 347–404. https://doi.org/10.1016/j.ocemod.2004.08.002

Skamarock, W. C., Klemp, J. B., Dudhia, J., Gill, D. O., Liu, Z., Berner, J., et al. (2021). A description of the advanced research WRF model version 4.3 (No. NCAR/TN-556+STR). https://doi.org/10.5065/1dfh-6p97

Sullivan, P. P., Banner, M. L., Morison, R. P., & Peirson, W. L. (2018). Turbulent flow over steep steady and unsteady waves under strong wind forcing. *Journal of Physical Oceanography*, *48*(1), 3–27. https://doi.org/10.1175/JPO-D-17-0118.1

Sullivan, P. P., McWilliams, J. C., & Patton, E. G. (2014). Large-eddy simulation of marine atmospheric boundary layers above a spectrum of moving waves. *Journal of the Atmospheric Sciences*, *71*(11), 4001–4027. https://doi.org/10.1175/JAS-D-14-0095.1

Taylor, P. K., & Yelland, M. J. (2001). The dependence of sea surface roughness on the height and steepness of the waves. *Journal of Physical Oceanography*, *31*(2), 572–590. https://doi.org/10.1175/1520-0485(2001)031⟨0572:TDOSSR⟩2.0.CO;2

Tewari, M., Chen, F., Wang, W., Dudhia, J., LeMone, M., Mitchell, K., et al. (2004). Implementation and verification of the unified NOAH land surface model in the WRF model. In *20th conference on weather analysis and forecasting/16th conference on numerical weather prediction* (pp. 11–15).

The WAVEWATCH III Development Group, W. (2019). *User manual and system documentation of WAVEWATCH III version 6.07* (Technical Note 333). NOAA/NWS/NCEP/MMAB.

Thompson, G., Field, P. R., Rasmussen, R. M., & Hall, W. D. (2008). Explicit forecasts of winter precipitation using an improved bulk microphysics scheme. Part II: Implementation of a new snow parameterization. *Monthly Weather Review*, *136*(12), 5095–5115. https://doi.org/10.1175/2008MWR2387.1

Tolman, H. L., Balasubramaniyan, B., Burroughs, L. D., Chalikov, D. V., Chao, Y. Y., Chen, H. S., & Gerald, V. M. (2002). Development and implementation of wind-generated ocean surface wave Modelsat NCEP. *Weather and Forecasting*, *17*(2), 311–333. https://doi.org/10.1175/1520-0434(2002)017⟨0311:DAIOWG⟩2.0.CO;2

Tomaszewski, J. M., & Lundquist, J. K. (2020). Simulated wind farm wake sensitivity to configuration choices in the Weather Research and Forecasting model version 3.8.1. *Geoscientific Model Development*, *13*(6), 2645–2662. https://doi.org/10.5194/gmd-13-2645-2020

Tracy, B. A., Devaliere, E., Hanson, J., Nicolini, T., & Tolman, H. (2007). Wind sea and swell delineation for numerical wave modeling (JCOMM Technical Report 41 Nos. 1442, Paper P12).

Vincent, L., & Soille, P. (1991). Watersheds in digital spaces: An efficient algorithm based on immersion simulations. *IEEE Transactions on Pattern Analysis and Machine Intelligence*, *13*(6), 583–598. https://doi.org/10.1109/34.87344

Warner, J. C., Sherwood, C. R., Arango, H. G., & Signell, R. P. (2005). Performance of four turbulence closure models implemented using a generic length scale method. *Ocean Modelling*, *8*(1), 81–113. https://doi.org/10.1016/j.ocemod.2003.12.003

Weatherall, P., Marks, K. M., Jakobsson, M., Schmitt, T., Tani, S., Arndt, J. E., et al. (2015). A new digital bathymetric model of the world's oceans. *Earth and Space Science*, *2*(8), 331–345. https://doi.org/10.1002/2015EA000107

Wu, C., Wang, Q., Luo, K., & Fan, J. (2022). Mesoscale impact of the sea surface on the performance of offshore wind farms. *Journal of Cleaner Production*, *372*, 133741. https://doi.org/10.1016/j.jclepro.2022.133741

Wu, L., Shao, M., & Sahlée, E. (2020). Impact of air–wave–sea coupling on the simulation of offshore wind and wave energy potentials. *Atmosphere*, *11*(4), 327. https://doi.org/10.3390/atmos11040327

Yang, H., Ge, M., Gu, B., Du, B., & Liu, Y. (2022). The effect of swell on marine atmospheric boundary layer and the operation of an offshore wind turbine. *Energy*, *244*, 123200. https://doi.org/10.1016/j.energy.2022.123200

Young, I. R. (1997). The growth rate of finite depth wind-generated waves. *Coastal Engineering*, *32*(2), 181–195. https://doi.org/10.1016/S0378-3839(97)81749-8

Zhao, B., Sahlée, E., Du, J., & Wu, L. (2024). Wind stress modification by offshore wind turbines: A numerical study of wave blocking impacts. *Ocean Engineering*, *313*, 119651. https://doi.org/10.1016/j.oceaneng.2024.119651